



Published in final edited form as:

Neuroimage. 2022 December 01; 264: 119701. doi:10.1016/j.neuroimage.2022.119701.

Slice-direction geometric distortion evaluation and correction with reversed slice-select gradient acquisitions

Anna I. Blazejewska^{a,b,*}, Thomas Witzel^c, Jesper L.R. Andersson^d, Lawrence L. Wald^{a,b,e}, Jonathan R. Polimeni^{a,b,e}

^aAthinoula A. Martinos Center for Biomedical Imaging, Massachusetts General Hospital, Charlestown, Boston, MA, USA

^bDepartment of Radiology, Harvard Medical School, Boston, MA, USA

^cQ Bio, Inc., Redwood City, CA, USA

^dWellcome Centre for Integrative Neuroimaging, FMRIB, Nuffield Department of Clinical Neurosciences, University of Oxford, Oxford UK

^eHarvard-MIT Division of Health Sciences and Technology, Massachusetts Institute of Technology, Cambridge, MA, United States

Abstract

Accurate spatial alignment of MRI data acquired across multiple contrasts in the same subject is often crucial for data analysis and interpretation, but can be challenging in the presence of geometric distortions that differ between acquisitions. It is well known that single-shot echo-planar imaging (EPI) acquisitions suffer from distortion in the phase-encoding direction due to B_0 field inhomogeneities arising from tissue magnetic susceptibility differences and other sources, however there can be distortion in other encoding directions as well in the presence of strong field inhomogeneities. High-resolution ultrahigh-field MRI typically uses low bandwidth in the slice-encoding direction to acquire thin slices and, when combined with the pronounced B_0 inhomogeneities, is prone to an additional geometric distortion in the slice direction as well. Here we demonstrate the presence of this slice distortion in high-resolution 7T EPI acquired with a novel pulse sequence allowing for the reversal of the slice-encoding gradient polarity that enables

This is an open access article under the CC BY-NC-ND license (<http://creativecommons.org/licenses/by-nc-nd/4.0/>)

*Corresponding author at: MGH Athinoula A. Martinos Center for Biomedical Imaging, Bldg 149 13th St Rm 2301, Charlestown MA, 02129 USA, ABLAZEJEWSKA@mgh.harvard.edu (A.I. Blazejewska).

Data and code sharing statement

The informed consent process approved by our local Institutional Review Board does not include any statement or clause indicating that the data will be shared to enable secondary uses, therefore data cannot be made openly available.

The data analysis presented in this manuscript used standard tools freely available in the FSL software package (<https://fsl.fmrib.ox.ac.uk/fsl/fslwiki/FSL>). The scripts including the specific commands used in this study are available under a license at <https://github.com/aib8/overeasy-topup>.

Credit authorship contribution statement

Anna I. Blazejewska: Conceptualization, Methodology, Formal analysis, Writing – original draft, Writing – review & editing. **Thomas Witzel:** Software. **Jesper L.R. Andersson:** Conceptualization, Methodology, Writing – review & editing. **Lawrence L. Wald:** Resources, Supervision. **Jonathan R. Polimeni:** Conceptualization, Methodology, Supervision, Funding acquisition, Writing – original draft, Writing – review & editing.

Supplementary materials

Supplementary material associated with this article can be found, in the online version, at doi:10.1016/j.neuroimage.2022.119701.

the acquisition of pairs of images with equal magnitudes of distortion in the slice direction but with opposing polarities. We also show that the slice-direction distortion can be corrected using gradient reversal-based method applying the same software used for conventional corrections of phase-encoding direction distortion.

1. Introduction

Many neuroimaging studies using MRI frequently leverage multiple imaging protocols with varying complementary contrasts. This can enable the extraction of more functional or structural information at any given anatomical location than what can be achieved with any single modality alone, which is a key advantage of MRI over other noninvasive imaging technologies. To achieve this, accurate alignment of these MRI data across the different contrasts acquired is critical. Head motion often occurs between scans, and rigid registration can be employed to align the datasets—by utilizing various available methods that can account for the different image contrasts—however this alignment is far more challenging in the presence of differential geometric distortion between these acquisitions. In many cases, these geometric distortions also can change with head position, further exacerbating error in alignment.

The most prevalent source of geometric distortion in MRI is inhomogeneity of the main magnetic field, B_0 , which for modern MRI scanners is predominantly induced by magnetic susceptibility differences within the volunteer's head mainly found in regions near to air-tissue interfaces (e.g. at the sinuses, ear canals, and oral cavity). These local magnetic field variations cause field gradients that interfere with the image encoding gradients and thereby result in errors in image encoding such as voxel shift errors, which manifest as nonrigid geometric distortion (i.e., local expansion or compression) of the resulting image. For a given local B_0 field offset, these image encoding errors scale with image encoding bandwidth, such that a lower encoding bandwidth results in a greater vulnerability to distortion and a larger voxel shift in the presence of field inhomogeneity.

Single-shot Echo Planar Imaging (EPI) is widely used for acquiring various MRI contrasts such as functional, diffusion and perfusion weighted imaging, and increasingly for anatomical imaging as well. EPI is well known to be vulnerable to these geometric distortions, which are primarily along the phase-encoding direction; in EPI, not only is this the encoding direction with the lowest bandwidth, but also in most applications of EPI the phase-encoding bandwidth is sufficiently low that distortions are clearly apparent, with maximum voxel displacements in the centimeter range. Phase encoding in EPI has relatively low encoding bandwidth (such as 30 Hz/pixel) compared to the relatively high frequency-encoding bandwidths typically used in conventional (non-EPI) acquisitions (such as 600 Hz/pixel), thus geometric distortion is most often considered to be only in the phase-encoding direction in EPI, and for most non-EPI applications distortion in the frequency-encoding direction is negligible (Jezzard, 2012). While the distortion in the phase-encoding direction in EPI can be partly mitigated with parallel imaging acceleration (de Zwart et al., 2002; Griswold et al., 1999), which increases the effective phase-encoding bandwidth, the undersampling used in accelerated acquisitions brings with it a fixed penalty

of decreased signal-to-noise ratio (SNR), and high acceleration factors can introduce severe artifacts even with modern receive coil arrays, therefore acceleration alone cannot fully remove the distortion in EPI. For this reason, EPI distortion must be addressed in post processing. Conventionally, post-hoc correction of the geometric distortion is performed based on an estimation of the voxel shifts induced by the B_0 magnetic field inhomogeneity during the image acquisition, where the field offsets can be calculated from a separately acquired B_0 map (Jezzard and Balaban, 1995). Another approach is based on the “reversed gradient” method that, instead of using an explicit B_0 field map, infers the distortion using a pair of two EPI scans acquired with the phase-encoding gradients played out with opposite polarities, resulting in two images with equal magnitudes of distortion but in opposite directions, from which non-linear image registration can be used to simultaneously estimate and correct the distortion (Andersson et al., 2003; Bowtell et al., 1994; Chang and Fitzpatrick, 1992; Holland et al., 2010; Morgan et al., 2004).

While distortion in the phase-encoding and frequency-encoding directions have been thoroughly considered in previous work, the distortion in the slice-encoding direction for 2D slice-by-slice imaging has until now received little attention (Studholme et al., 2000), but is becoming more important as it may be increasingly present in modern MRI applications. For example, high-resolution (sub-millimeter) fMRI uses thin imaging slices which are usually acquired by maximizing slice-select gradient strength; however once the maximum strength is reached, a decrease of the slice-encoding gradient bandwidth is required to further narrow the range or excited frequencies, which could lead to the additional geometric distortions and “slice bending” in the slice direction. For conventional slice-selective pulses, slice thickness (TH) is determined by the slice-encoding gradient strength (G_z) and slice-select RF pulse bandwidth (BW) such that $TH=BW/\gamma G_z$. While the value of G_z is usually dictated by the desired slice thickness, the RF pulse bandwidth is related to the pulse duration (D) and the time-bandwidth product (TBW), i.e., $TBW \equiv D \cdot BW$. In sub-millimeter imaging, because G_z typically cannot be further increased, the slice thickness can be decreased by modifying the RF pulse design either by reducing TBW (which leads to degradation of the slice profile), or by increasing the pulse duration (which lowers SAR but increases the minimal echo time, TE). Thus, to decrease slice thickness, often one must resort to reducing the RF excitation pulse bandwidth. While stronger gradient coils help to achieve distortion-free thin slices, they bring a penalty of increased peripheral nerve stimulation and potential eddy currents. High-resolution fMRI is commonly performed at ultra-high magnetic field strengths (> 7 T) where susceptibility-induced B_0 field inhomogeneities are stronger than at conventional field strengths, suggesting that this imaging modality may be particularly vulnerable to slice distortion. In addition, in many applications a low slice-select RF pulse bandwidth may also be desirable to decrease power deposition (SAR). Slice distortion due to field inhomogeneity has previously been reported in MRI studies conducted using conventional field strengths as well (such as 1.5 T) (Sumanaweera et al., 1993) and in the presence of metal implants where magnetic susceptibility offsets are substantially higher than those between different tissue types (Hargreaves et al., 2011; Hopper et al., 2006; Lu et al., 2009).

To characterize this slice distortion and present a method for correcting it, here we use a novel acquisition that acquires pairs of images with reversed polarity of the slice-encoding

gradient to create image pairs with equal slice distortions in opposing directions, and then demonstrate that typical 7T fMRI acquisitions do suffer from noticeable geometric distortion in the slice-encoding direction, which will result in alignment errors when registering these data to other datasets, e.g., to anatomical reference data typically acquired using 3D encoding. Our method is analogous to the reversed-gradient method used for removing distortion in the phase-encoding or frequency-encoding directions, and here it is applied in the slice-encoding direction. We demonstrate a correction of these slice distortions with our method, and evaluate it using both spin-echo (SE) or gradient-echo (GE) based data acquired with slice gradients and RF pulse (excitation and refocusing) bandwidths that are matched those used in the target fMRI protocol. Because we use, for correction, the popular *topup* method implemented in the FSL package (Andersson et al., 2003; Smith et al., 2004), we have named our method *overeasy* (Blazejewska et al., 2017). While we demonstrate our approach using high-resolution EPI data, it is applicable to any 2D multi-slice data suffering from geometric distortion in the slice direction, which becomes more pronounced at higher spatial resolutions and higher magnetic field strengths.

2. Materials and methods

Seven healthy volunteers (4F/3M, 26±7 y.o.) participated in this study after providing written informed consent in accordance with our institution's Human Research Committee; the study protocol was approved by the Institutional Review Board of Massachusetts General Hospital.

All data were acquired on a whole-body 7T scanner (MAGNETOM, Siemens Healthcare, Erlangen, Germany) equipped with a “short-z FOV” body gradient coil (SC72) and an inhouse-built 32-channel coil array for receive and a single-channel birdcage coil for transmit (Keil et al., 2010). During each experimental session multiple EPI scans were acquired following standard automatic B_0 shimming.

The *overeasy* method used in this study consists of acquiring pairs of EPI data with reversed slice-select gradient polarity, with appropriate shifting of the RF pulse center frequency, which causes the voxel displacement direction to alternate between the two acquisitions, as illustrated in Fig. 1. Note that the images were not acquired purely axially, and were tilted somewhat to be roughly aligned to the brain's AC-PC axis, therefore the slice-select gradient was not along a single gradient axis thus the gradient was a combination of the physical G_x , G_y and G_z gradients. Because the only parameter to change between this pair of images is the slice-select gradient polarity, the differential distortion between these images is in the direction perpendicular to the slice plane. Because these two images are acquired immediately after one another, we assume that the B_0 inhomogeneity is identical between the two acquisitions, as is common for reversed-gradient methods. For each scanning session an additional B_0 field map was also obtained for validation. See Table 1 for details of the scanning parameters.

Both GE and SE variants of the *overeasy* acquisition were tested, each with similar EPI readouts and slice bandwidths. The spin-echo EPI may be advantageous over gradient-echo

EPI at 7T because of the potential for through-slice dephasing in the gradient-echo, which could cause signal loss exactly in those regions that suffer the most from distortion.

Each EPI scan consisted of 5 repetitions (for noise averaging) and the two slice-encoding polarity scans were acquired consecutively. Both the SE and GE EPI data were acquired near-axially (see above) at 1.5 mm in-plane resolution and a slice thickness of 1 mm using TBW=2.6. To demonstrate the effect of slice bandwidth on the slice distortion, we acquired multiple runs with RF pulse durations $D=6, 8$ and 10 ms (which corresponds to BW=433, 325 and 260 Hz, respectively), and for a subset of four subjects the GE data with TBW=5.2 and 7.2 and $D=10$ ms (BW=520 and 720 Hz, respectively).

(Recall that the distortion in the slice-encoding direction in units of “*slice-thicknesses*” is characterized by the slice-encoding bandwidth BW (e.g., if the slice-select RF pulse bandwidth is 260 Hz, and there is a local B_0 field inhomogeneity corresponding to an offset of 520 Hz, the resulting slice displacement or distortion will be two slice-thicknesses, equivalent to twice the thickness of the slice); however, the distortion in the slice-encoding direction in units of *millimeters* is characterized by the slice-select gradient amplitude G_z (see appendix of Polimeni et al., 2018).)

To test whether the *overeasy* method could be used to simultaneously estimate slice-encoding distortion and phase-encoding distortion, for a subset of 5 subjects we also acquired SE EPI data where we alternated both the slice-select gradient polarity and the phase-encoding gradient polarity. These data were acquired with 2 mm in-plane resolution and 1-mm slice thickness using TBP=2.6 and $D=10$ ms, with alternating phase-encoding directions: anterior-to-posterior and posterior-to-anterior (four datasets in total).

To allow us to directly compare the distortion-correction results across all acquired slice-encoding bandwidths and between the SE and GE EPI data, for each subject all datasets acquired with positive slice-encoding gradients were co-registered together and then all datasets acquired with negative slice-encoding gradients were co-registered together using rigid (i.e., 6 degrees of freedom) registration calculated using the FLIRT tool of the FSL software package (Jenkinson et al., 2002; Jenkinson and Smith, 2001). The voxel shift deformation fields were calculated for each reversed slice-encoding volume pair using the *topup* reversed-gradient method as implemented in FSL (Andersson et al., 2003; Smith et al., 2004) from SE and GE data separately. While *topup* is mainly intended for correcting distortion along the phase-encoding direction, it is possible to use this software to correct distortion in any encoding direction, therefore no modifications to the software were needed. The *topup* method jointly performs distortion and motion correction of the input dataset to account for potential distortion-independent shifts between volumes acquired with reversed slice-encoding gradient polarities; this effectively provides a co-registration across positive and negative slice-encoding gradient polarity volume pairs, ignoring only potential motion in the targeted direction of distortion. Two distortion correction approaches were evaluated and applied to GE EPI data: (1) using the voxel shifts in the slice direction estimated from the SE EPI *overeasy* pairs, consistent with the typical use case of the *topup* method, and (2) using voxel shifts in the slice direction estimated from the GE EPI data themselves, to test whether any signal loss present due to through-slice dephasing would bias the results.

Slice-distortion can also be estimated using a conventional B_0 field map, provided that the slice-encoding bandwidth, slice thickness and gradient direction are known, and this distortion estimate should be equivalent to that given by *overeasy*. Therefore, to validate the *overeasy*-based correction, voxel shift maps based on separately acquired B_0 field map scans resampled to the EPI space were calculated, then distorted along the EPI phase-encoding direction so that they more accurately matched the distorted EPI data. The resulting voxel shift maps were estimated for different TBW and D combinations and compared pair-wise with those estimated from the corresponding *overeasy* data at a voxel-by-voxel basis, and the consistency between these two estimates was evaluated by calculating the correlation coefficient between the B_0 - fieldmap-based and the *overeasy*-based estimates.

Finally, a two-step distortion correction approach was used to correct distortion in both the phase-encoding and slice-encoding directions in an additional SE EPI dataset acquired with two pairs of reversed gradient directions—i.e., the SE EPI data were acquired four times, with both positive and negative phase-encoding and slice-encoding directions. For this two-step 2D correction, the phase-encoding distortion correction was performed first, then, in a subsequent separate step, the slice-encoding distortion correction was applied to the phase-encoding-direction-corrected data.

3. Results

We found clear geometric distortion to occur in the slice-encoding direction in all GE and SE EPI datasets acquired with the proposed *overeasy* method which allows for reversing slice-select gradient polarity, as illustrated in Fig. 1. Example pairs of images with alternating slice-encoding directions are shown in Fig. 2, where distortions up to several slice-thicknesses are observable in regions of strong B_0 field inhomogeneity. The regions near the frontal sinus where distortion is the most severe were magnified to visualize the magnitude of voxel shifts; to aid in the visual inspection of these displacements, a horizontal red line—placed in the same location in scanner coordinates across the two images of the *overeasy* pairs—is included as a reference. This simple reversal of the slice-encoding gradient polarities added into the pulse sequences provides a concrete demonstration of the slice-distortion effect. We then corrected the slice-select direction distortion in the *overeasy* pairs of images by applying *topup* method, where either SE or GE EPI reference data of opposite slice-encoding gradient polarities were used to derive a deformation field (Fig. 3).

Fig. 2 presents representative example sagittal reformats of the original distorted GE EPI data acquired with TBW=2.6 and D =10 ms (BW=260 Hz) with positive and negative gradient polarities (marked with red arrows at the images) for three different subjects, together with the corrected data based on either the deformation estimated from the SE EPI data or from the GE EPI data themselves. An overview of the distorted and corresponding corrected data for all remaining subjects is presented in Supplementary Fig. 1.

As expected, the extent of distortion in the slice-encoding direction was the most pronounced in the images acquired with the lowest slice-encoding bandwidth of 260 Hz, which corresponded to TBW of 2.6 and D of 10 ms, and gradually decreased with increasing bandwidth values. Fig. 3 presents a comparison of the example sagittal reformats from

oblique-axial GE and SE EPI datasets acquired for one subject with different BW values ranging from 260 to 720 Hz, and both positive and negative slice-encoding gradient polarity. A summary of the examples for all the datasets and the corresponding distortion corrected slices from all remaining subjects can be found in Supplementary Fig. 2.

Voxel-shifts in the slice-encoded direction were averaged across all subjects for the data acquired with BW=260 Hz; in summary, the 95th percentile of displacements within the brain was greater than 0.4 mm for the GE-based correction and greater than 0.5 mm for the SE-based correction, which in both cases corresponds to about half of the slice thickness. Summarized in another way, ~4,500 voxels (or 0.8% of the image volume within the brain) for GE-based correction and ~7,700 voxels (or 1.4% of the image volume within the brain) for SE-based correction were shifted by one slice thickness or more (i.e., 1 mm or more). Considering that average cortical thickness is about 2 mm across the brain, these shifts could have a significant impact on the fMRI results in the regions of most severe distortion (such as orbitofrontal cortex and temporal poles).

Slight differences between GE- and SE-based voxel shift maps were likely due to through-plane dephasing and signal loss in GE EPI data; the larger displacements estimated from the SE EPI data supports this interpretation and suggests that the SE EPI data provides more accurate distortion estimates. However, since the largest voxel displacements were found within regions of severe dephasing and signal loss in the GE EPI data, mis-estimating distortions in regions without appreciable signal may be tolerable in some applications. Indeed, the results of correcting the GE EPI data using distortion estimates from either the GE EPI data themselves or from the matched SE EPI data were nearly identical. Therefore, while SE EPI is expected to provide more accurate distortion estimates, and thus is recommended in most cases, for correcting distortion in GE EPI data both approaches to estimating distortion are expected to yield similar outcomes. Fig. 4 summarizes the correlations between the voxel shift maps resulting from both *topup* approaches and the voxel shift map derived from the field map scan with values similar for SE- and GE-*topup*.

All voxel shift maps generated using *topup* and calculated from the separately acquired B_0 field map scans demonstrated similar spatial distribution of the shift values, reaching ± 2 mm which corresponds to twice the slice thickness, as can be seen in Fig. 4A for a representative subject. The correlation coefficients calculated between *topup* and field map-based maps within the brain mask were highest for the lowest BW values (the most distorted datasets) reaching 0.58–0.82 (Figures 4A & B) and the correlation coefficient decreased with the increasing BW. The lower correlation coefficient seen for the data with the lowest level of distortion is likely due to the smaller displacements estimated in the presence of noise (i.e., lower “displacement-to-noise ratio”). The mean values of absolute voxel shifts calculated within the brain were also similar for both approaches, with *topup* estimations being slightly higher overall and SE-*topup* estimations being slightly higher than GE-*topup* (Fig. 4C). Images acquired with lower slice-encoding bandwidth demonstrated larger mean absolute voxel shift values (Fig. 4C) over larger spatial area of the brain (Fig. 4A) with the decreasing trend for increasing BWs, as expected.

We also demonstrated a two-step approach using *topup* to correct distortion in phase-encoding and slice-select direction applied to four SE EPI volumes acquired separately with A→P and P→A phase-encoding gradient direction, and positive and negative slice-encoding gradient direction (Fig. 5).

4. Discussion

In this work we presented a simple method for quantifying distortion in the slice-select direction, and demonstrated that modern high-resolution (i.e., thin-sliced) 7T fMRI data contain observable geometric distortion in the slice direction, with a voxel shifts that may exceed the slice thickness. We were able to measure these distortions from either SE or GE-based acquisitions, indicating that for these thin-slice protocols through-slice dephasing does not prevent reasonably accurate estimations from GE-based data, although whether this finding generalizes to other GE-based protocols will depend on several factors including slice thickness, TE, slice prescription, brain region, and B_0 shim quality. While these slice-encoding distortions are smaller in magnitude than the well-known phase-encoding distortions, for accurate alignment of data across different MRI data, such as alignment of 2D EPI data to 3D anatomical reference data, slice distortion must be addressed to ensure accuracy of the alignment.

While slice distortion can be readily estimated using conventional B_0 field map methods, provided that the slice-select bandwidth and gradient direction are known, here we used a simple approach to demonstrate in a concrete way the level of slice-distortion that does not require any knowledge of the RF pulses. Our method, based on pairs of EPI data, is faster than conventional methods that acquire an explicit B_0 field map, which generally require multiple minutes, making them less practical—especially in cases where estimating distortion multiple times during a session is desirable, which may be the case in subjects prone to motion. Because magnetic-susceptibility-induced B_0 inhomogeneity changes with head position, and, in particular, with head orientation relative to the B_0 axis, updating the B_0 inhomogeneity and the associated image distortion periodically during the imaging session can help ensure consistent accuracy of the correction throughout the session. EPI-based field maps are another possibility and have some advantages over B_0 field maps acquired with conventional encoding (Hutton et al., 2002), provided that the distortions are not too severe. These have also been extended to estimating dynamic changes in distortion during fMRI runs (Lamberton et al., 2007). Still, an advantage of acquiring pairs of reverse-gradient images is that it provides a means to validate distortion correction based on conventional B_0 field maps: if the B_0 field map yields an accurate estimate of the image distortion, applying the B_0 - fieldmap-based correction to each image of the reversed-gradient pair should result in two identical corrected images. Also, it is possible to estimate slice-encoding distortion present in conventional (i.e., non-EPI) image encoding methods as well using the *overeasy* method, time permitting, if the slice-select RF pulse bandwidth and slice thickness can be set to be identical to that of the target acquisition.

Another important advantage of reverse-gradient methods for estimating slice-encoding distortion is that they can also help remove distortions due to eddy currents. Since the slice-select gradient amplitude can be larger than other gradient blips, it can be a source of eddy

currents that induce B_0 inhomogeneity in the image and therefore distortion (Varadarajan et al., 2021). Reversing the slice-encoding gradient will reverse the eddy currents and therefore both eddy current and susceptibility distortions can be corrected. This is challenging to achieve with conventional B_0 field maps, unless again the B_0 field map uses the same slice-select gradient as the target acquisition so that both the B_0 field map and the target acquisition experience the same eddy currents from the slice-select gradient, which would allow the B_0 field map to measure the same B_0 inhomogeneity (due to both eddy currents and susceptibility gradients) that is present during the target acquisition.

When B_0 inhomogeneity becomes severe, the distortions along the phase-encoding direction can grow sufficiently large as to induce “singularities” in the EPI data where the compressive distortion results in what is known as “voxel pile-up” artifacts. These artifacts cannot be corrected when using a single phase-encoding polarity, but they can be resolved when reversed-gradient pairs are available. In principle it is possible for “slice pile-up” to occur, although given that the slice-encoding bandwidth is considerably higher (20 times and more) than typical phase-encoding bandwidths this is unlikely. In more moderate cases, B_0 inhomogeneity will cause a spatially-varying voxel size in the phase-encoding direction, due to the geometric expansion and compression of the image (Wang et al., 2022). While B_0 inhomogeneity is often viewed as causing mainly a shift in the slice position, if the B_0 field changes *within the slice* along the slice direction it can similarly cause an expansion or compression. However, given that relatively low slice-encoding bandwidths are mainly used to achieve thin slices, and the B_0 field is generally smoothly varying in space, it is also unlikely that the B_0 field will change considerably at the spatial scale of these thin slices. Future work will consider the effects of B_0 inhomogeneity on the true resolution of the image in the slice direction.

Related artifacts are also expected in 3D imaging using slab-selective pulses. The spatial extent of local B_0 offsets or gradients in the brain is typically larger than the thickness of a 2D slice but will be smaller than the thickness of a 3D slab. If the intended borders of the slab were to pass through a region of strong B_0 offset (e.g., around the frontal sinuses), there the slab border would be shifted in the slab-encoding direction by an amount that depends on the slab-select gradient amplitude and the magnitude of the B_0 offset. This would lead to either a local expansion or compression of the excited slab at the location of the B_0 offset. Note that this local shift in (or distortion of) the slab boundary results in a change in the spatial extent of excited spins, but not in any distortion or displacement of spatial encoding. However, artifacts may still occur. If locally the spatial extent or thickness of the excited slab is much thinner than desired, signal loss will be seen in regions where spins were not excited. If locally the spatial extent or thickness of the excited slab is much thicker than desired, spins outside of the partition-encoded (a.k.a., secondary/3D phase-encoded) region can be excited, leading to wrap-around artifacts in the partition-encoded direction; oversampling in the slab-encoding direction can help mitigate these artifacts. In other words, in 2D imaging, spatial encoding in the z direction is performed with slice selection, while in 3D imaging spatial encoding in the z direction is performed with partition-encoding gradients, and these partition-encoding gradients are typically (for conventional acquisitions) immune to spatial localization or displacement errors. While for 2D imaging each individual slice position is shifted due to local B_0 offsets—which induces distortion in the stack of

image slices—for 3D imaging, generally only the borders of the excited slab are shifted, and no voxel displacements are induced per se. If only a single slab is excited, our *overeasy* approach cannot correct these artifacts. (Similarly, *overeasy* cannot correct slice-encoding distortions when only a single 2D slice is acquired.) Nevertheless, our approach could be used to detect slab profile distortion and associated artifacts by comparing a pair of slabs acquired with reversed slab-encoding gradient polarities by identifying brain regions that are inconsistent between the corresponding image pairs.

A final practical consideration is on how to apply this distortion correction to the data. While here the image pairs were corrected directly, using a nonlinear warping followed by an interpolation, in practice, especially in high-resolution applications, it is preferable to mathematically compose all transformations of the data to minimize the number of interpolation steps (Glasser et al., 2013; Polimeni et al., 2018). Because the distortion in the slice-encoding direction will typically be far smaller than that of the phase-encoding direction, most of the displacements in the slice-encoding direction will likely be sub-voxel shifts, which will induce blurring when interpolation is performed. Higher-order interpolation, combined with image grid upsampling, can also help mitigate resolution losses due to interpolation.

Here we focused on demonstrating the distortion in the slice-encoding direction by reversing the gradient polarity of the slice-select gradient, and demonstrated that the bandwidths used in modern fMRI acquisitions do lead to perhaps unexpectedly large levels of distortion the slice direction. This approach can be combined with existing reverse-gradient methods that reverse the phase-encoding direction, as we demonstrated above (see Fig. 5). While here we acquired four images, but reversing each gradient direction, in principle only one pair is needed, e.g., a positive-slice-encode and positive-phase-encode image followed by a negative-slice-encode and negative-phase-encode image, to save time. In this case, the differential distortion between the two images is no longer constrained to be only along the slice-encoding direction or along the phase-encoding direction, rather it would be at an angle partway between these two directions, where this angle would depend on the ratio of the bandwidths. For example, if the phase-encoding direction was in y , the slice-encoding in z , and the phase-encoding bandwidth were 5 times larger than the slice-encoding bandwidth, the differential distortion between the two images of the pair would be along a line about $\tan^{-1}(1/5) = 11^\circ$ off of the y axis. Another potential extension of this approach could be a dynamic distortion correction of the fMRI timeseries data that accounts for changing magnetic field offsets in the brain caused by effects such as breathing and head motion (Andersson et al., 2018).

5. Conclusions

Distortion in the slice-encoding direction up to several millimeters was detected in data acquired at 7T using a standard high-resolution fMRI protocol. Reducing bandwidth in the slice-encoding direction allows for acquiring thin slices but introduces vulnerability to geometric distortion due to B_0 inhomogeneity. While this distortion is lower than that found in the phase-encoding direction, it is large enough to reduce accuracy in the alignment of data acquired using different protocols. Both GE and SE EPI acquisitions were used

to acquire reversed-gradient data by alternating the polarity of the slice-encoding gradient along with the RF pulse frequency offset. These pairs of data allowed distortion correction using a conventional reverse-gradient method, implemented in *topup*. This slice-encoding gradient reversal can also be used as a means to validate geometric distortion correction based on acquired B_0 field maps. The proposed reversed-gradient-based distortion correction methods, termed *overeasy*, is beneficial in that it reduces the scan time needed to estimate distortion, just as existing EPI-based reversed-gradient methods do for phase-encoding distortion correction, and helps ensure that the relevant distortions from both susceptibility effects and eddy currents are estimated properly.

Supplementary Material

Refer to Web version on PubMed Central for supplementary material.

Acknowledgements

Special thanks to Ned Ohringer and Kyle Droppa for help with subject recruitment, to Azma Mareyam and Dr. Jason Stockman for hardware support, to Drs. Avery Berman, Yulin Chang, and Daniel Park for assistance in pulse sequence development, and to Dr. Mukund Balasubramanian for helpful discussions. This research has been supported by the NIH NIBIB (P41-EB015896, P41-EB030006 and R01-EB019437), by the NIMH (R01-MH124004), by the BRAIN Initiative (NIMH R01-MH111419, K99-MH120054 and R00-MH120054), and by the Athinoula A. Martinos Center for Biomedical Imaging, and made possible by NIH Shared Instrumentation Grants S10-RR023401, S10-RR023043 and S10-RR020948.

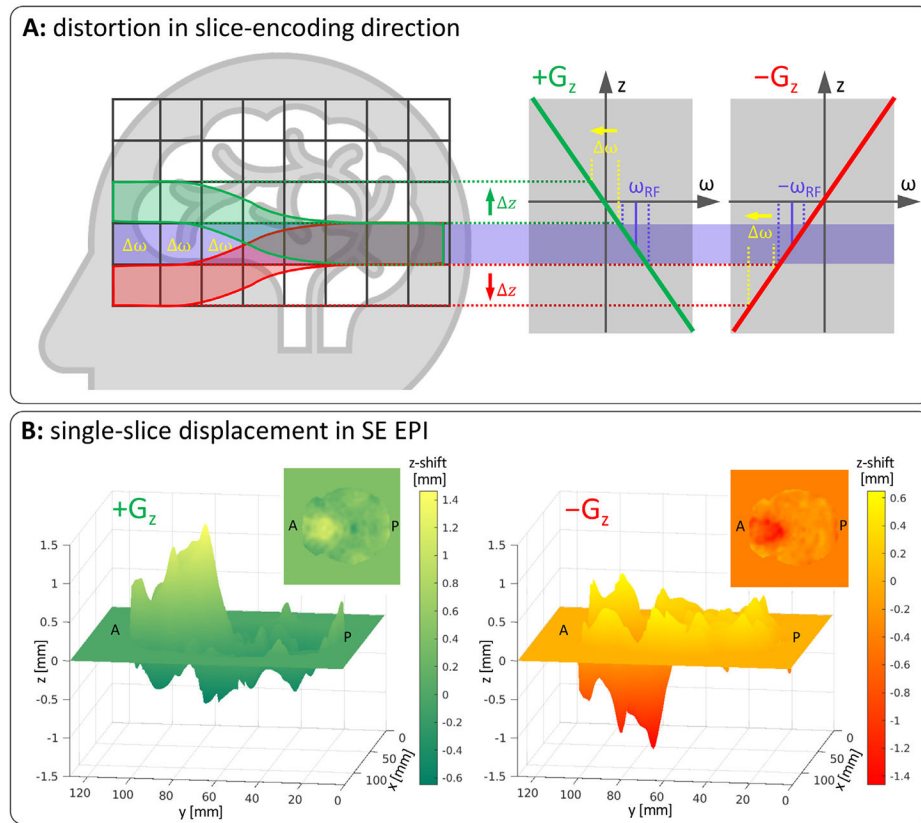
Data Availability

The authors do not have permission to share data.

References

- Andersson JLR, Graham MS, Drobnjak I, Zhang H, Campbell J, 2018. Susceptibility-induced distortion that varies due to motion: correction in diffusion MR without acquiring additional data. *Neuroimage* 171, 277–295. doi:10.1016/j.neuroimage.2017.12.040. [PubMed: 29277648]
- Andersson JLR, Skare S, Ashburner J, 2003. How to correct susceptibility distortions in spin-echo echo-planar images: application to diffusion tensor imaging. *Neuroimage* 20, 870–888. doi:10.1016/S1053-8119(03)00336-7. [PubMed: 14568458]
- Blazejewska AI, Witzel T, Wald LL, Polimeni JR, 2017. Correction of EPI geometric distortion in slice direction using reversed slice-select gradients and topup. *Proc. Int. Soc. Magn. Reson. Med* 25, 1650.
- Bowtell RW, McIntyre DJO, Commandre M-J, Glover PM, Mansfield P, 1994. Correction of geometric distortion in echo planar images. *ISMRM* 441.
- Chang H, Fitzpatrick JM, 1992. A technique for accurate magnetic resonance imaging in the presence of field inhomogeneities. *IEEE Trans. Med. Imaging* 11, 319–329. doi:10.1109/42.158935. [PubMed: 18222873]
- de Zwart JA, Van Gelderen P, Kellman P, Duyn JH, 2002. Application of sensitivity-encoded echo-planar imaging for blood oxygen level-dependent functional brain imaging. *Magn. Reson. Med* 48, 1011–1020. doi:10.1002/mrm.10303. [PubMed: 12465111]
- Glasser MF, Sotiropoulos SN, Wilson JA, Coalson TS, Fischl B, Andersson JL, Xu J, Jbabdi S, Webster M, Polimeni JR, Van Essen DC, Jenkinson M, 2013. The minimal preprocessing pipelines for the human connectome project. *Neuroimage* 80, 105–124. doi:10.1016/j.neuroimage.2013.04.127. [PubMed: 23668970]
- Griswold MA, Jakob PM, Chen Q, Goldfarb JW, Manning WJ, Edelman RR, Sodickson DK, 1999. Resolution enhancement in single-shot imaging using simultaneous acquisition

- of spatial harmonics (SMASH). *Magn. Reson. Med* 41, 1236–1245. doi:10.1002/(SICI)1522-2594(199906)41:6<1236::AID-MRM21>3.0.CO;2-T. [PubMed: 10371457]
- Hargreaves BA, Worters PW, Pauly KB, Pauly JM, Koch KM, Gold GE, 2011. Metal-induced artifacts in MRI. *Am. J. Roentgenol* 197, 547–555. doi:10.2214/AJR.11.7364. [PubMed: 21862795]
- Holland D, Kuperman JM, Dale AM, 2010. Efficient correction of inhomogeneous static magnetic field-induced distortion in echo planar imaging. *Neuroimage* 50, 1–18. doi:10.1016/j.neuroimage.2009.11.044. [PubMed: 20004249]
- Hopper TAJ, Vasili B, Pope JM, Jones CE, Epstein CL, Song HK, Wehrli FW, 2006. Experimental and computational analyses of the effects of slice distortion from a metallic sphere in an MRI phantom. *Magn. Reson. Imaging* 24, 1077–1085. doi:10.1016/j.mri.2006.04.019. [PubMed: 16997078]
- Hutton C, Bork A, Josephs O, Deichmann R, Ashburner J, Turner R, 2002. Image distortion correction in fMRI: a quantitative evaluation. *Neuroimage* 16, 217–240. doi:10.1006/nimg.2001.1054. [PubMed: 11969330]
- Jenkinson M, Bannister P, Brady M, Smith S, 2002. Improved optimization for the robust and accurate linear registration and motion correction of brain images. *Neuroimage* 17, 825–841. [PubMed: 12377157]
- Jenkinson M, Smith S, 2001. A global optimisation method for robust affine registration of brain images. *Med. Image Anal* 5, 143–156. [PubMed: 11516708]
- Jezzard P, 2012. Correction of geometric distortion in fMRI data. *Neuroimage* 62, 648–651. doi:10.1016/j.neuroimage.2011.09.010. [PubMed: 21945795]
- Jezzard P, Balaban RS, 1995. Correction for geometric distortion in echo planar images from B0 field variations. *Magn. Reson. Med* 34, 65–73. [PubMed: 7674900]
- Keil B, Triantafyllou C, Hamm M, Wald LL, 2010. Design optimization of a 32-channel head coil at 7T. *Intl Soc Mag Reson Med* 1493.
- Lamberton F, Delcroix N, Grenier D, Mazoyer B, Joliot M, 2007. A new EPI-based dynamic field mapping method: application to retrospective geometrical distortion corrections. *JMRI* 26, 747–755. doi:10.1002/jmri.21039. [PubMed: 17729370]
- Lu W, Pauly KB, Gold GE, Pauly JM, Hargreaves BA, 2009. SEMAC: slice encoding for metal artifact correction in MRI. *Magn. Reson. Med* 62, 66–76. doi:10.1002/mrm.21967. SEMAC. [PubMed: 19267347]
- Morgan PS, Bowtell RW, McIntyre DJO, Worthington BS, 2004. Correction of spatial distortion in EPI due to inhomogeneous static magnetic fields using the reversed gradient method. *JMRI* 19, 499–507. doi:10.1002/jmri.20032. [PubMed: 15065175]
- Polimeni JR, Renvall V, Zaretskaya N, Fischl B, 2018. Analysis strategies for high-resolution UHF-fMRI data. *Neuroimage* 168, 296–320. doi:10.1016/j.neuroimage.2017.04.053. [PubMed: 28461062]
- Smith SM, Jenkinson M, Woolrich MW, Beckmann C, Behrens TEJ, Johansen-Berg H, Bannister PR, De Luca M, Drobnjak I, Flitney DE, Niazy RK, Saunders J, Vickers J, Zhang Y, De Stefano N, Brady JM, Matthews PM, 2004. Advances in functional and structural MR image analysis and implementation as FSL. *Neuroimage* 23 (Suppl 1), S208–S219. [PubMed: 15501092]
- Studholme C, Constable RT, Duncan JS, 2000. Accurate alignment of functional EPI data to anatomical MRI using a physics-based distortion model. *IEEE Trans. Med. Imaging* 19, 1115–1127. doi:10.1109/42.896788. [PubMed: 11204849]
- Sumanaweera TS, Glover GH, Sumanaweera TO, Adler JR, 1993. MR susceptibility misregistration correction. *IEEE Trans. Med. Imaging* 12, 251–259. doi:10.1109/42.232253. [PubMed: 18218412]
- Varadarajan D, Balasubramanian M, Park DJ, Witzel T, Stockmann JP, Polimeni JR, 2021. Characterizing the acquisition protocol dependencies of B0 field mapping and the effects of eddy currents and spoiling. *Proc. Int. Soc. Magn. Reson. Med* 29, 3552.
- Wang J, Nasr S, Roe AW, Polimeni JR, 2022. Critical factors in achieving fine-scale functional MRI: removing sources of inadvertent spatial smoothing. *Hum. Brain Mapp* 3311–3331. doi:10.1002/hbm.25867. [PubMed: 35417073]

**Fig. 1.**

(A) Explanation of slice-encoding distortion due to local B_0 field offsets and the reverse-gradient method applied to the slice-select direction. The slice-select gradient establishes a mapping between frequency and position along the slice-select direction (here, the z direction). A given slice location is excited by an RF pulse at the corresponding frequency. In the absence of local B_0 field offsets, either a positive z gradient ($+G_z$) or a negative z gradient ($-G_z$) can be applied, and the desired slice location can be excited with an RF pulse using the appropriate center frequency, $+\omega_{RF}$ or $-\omega_{RF}$, respectively. In the presence of local B_0 field offsets, the location of the excited slice will be shifted, and the direction of the shift will depend on the polarity of the slice-selective gradient. In this case, the direction of the shift will depend on whether the $+G_z$ gradient or the $-G_z$ gradient is used, and the magnitude of the shift will depend on the local B_0 field offset ω as well as the gradient amplitude and the RF pulse bandwidth. A desired slice location without the shift is marked with purple, while actual slice locations with the shift occurring in presence of $+G_z$ and $-G_z$ are marked with green and red, respectively. (B) Example of distortion-induced displacement (z -shift) of the voxels in the slice-encoding direction within a single axial slice, caused by local B_0 field offsets, for images acquired with two opposite slice-encoding gradient polarities. In this example the shift is largest in the region at the front of the brain (near the frontal sinuses), and manifests as a positive z -shift when using the $+G_z$ gradient and a negative z -shift when using the $-G_z$ gradient.

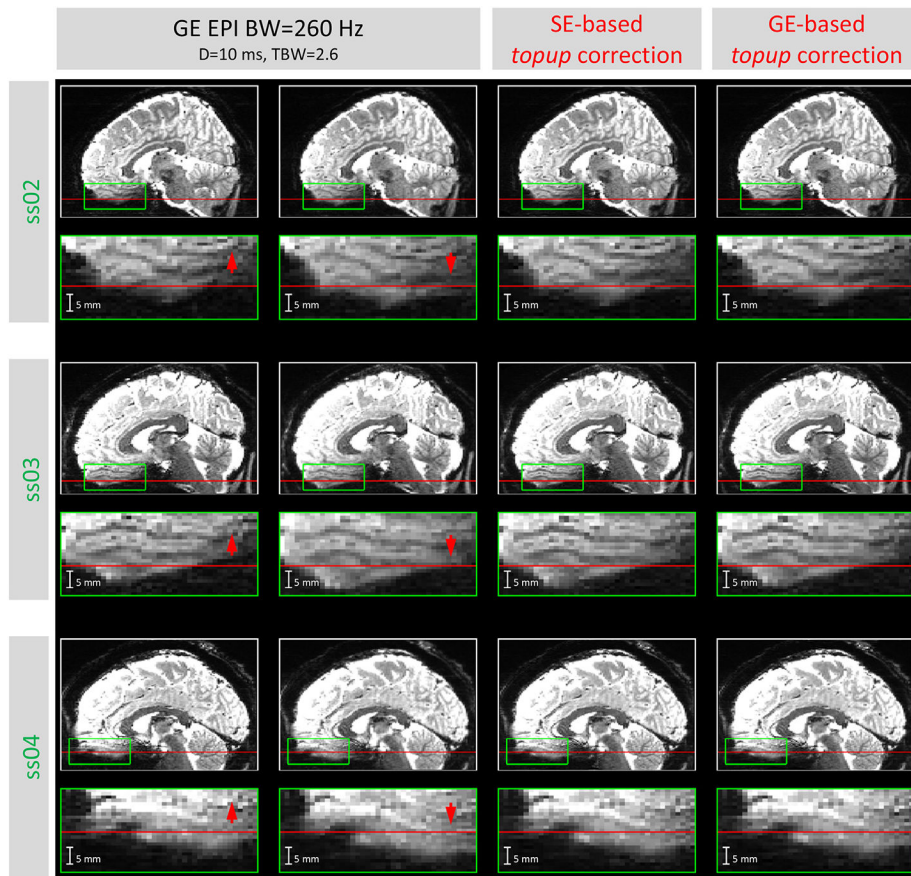


Fig. 2. Example sagittal reformats of oblique-axial GE EPI datasets from three different subjects (ss02, ss03 and ss04), acquired with 1-mm slice thickness, 1.5-mm in-plane resolution, positive and negative slice-encoding gradient direction, slice-encoding pulse duration $D=10$ ms and $TBW=2.6$, which corresponds to $BW=260$ Hz (left). The positive ($+G_z$) and negative ($-G_z$) slice encoding directions are indicated by red arrows. Corresponding slices distortion-corrected using SE-based (middle) and GE-based (right) data. The green box represents the regions shown in the magnified inserts, which show distortion in the slice-encoding direction in the frontal sinus region, and the red horizontal line is positioned at the same location in all images as a reference to help visualize the amount of displacement in the image data. The corresponding images for all remaining subjects and BW values tested are presented in Supplementary Fig. 1.

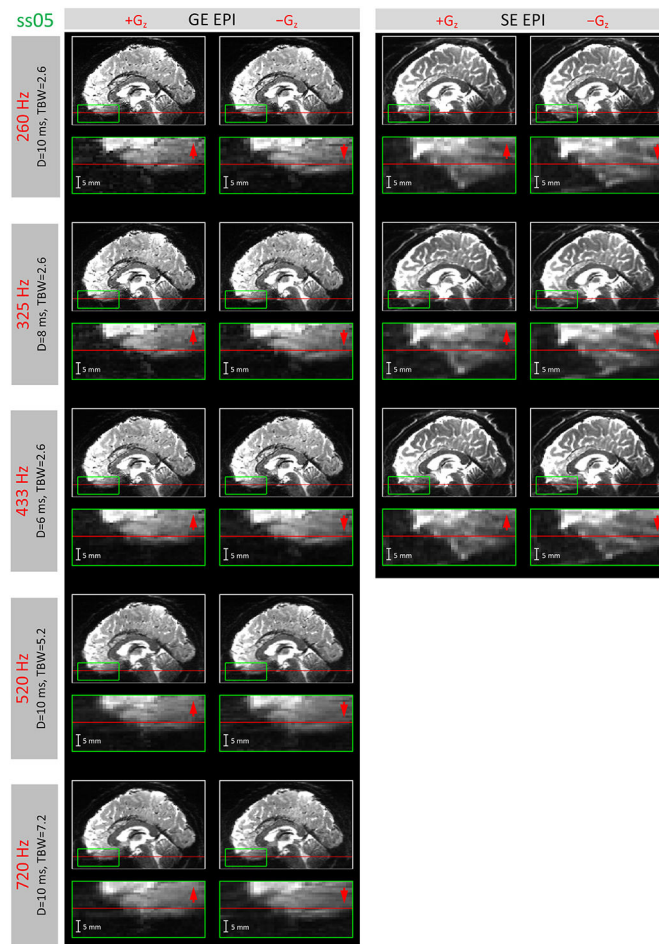
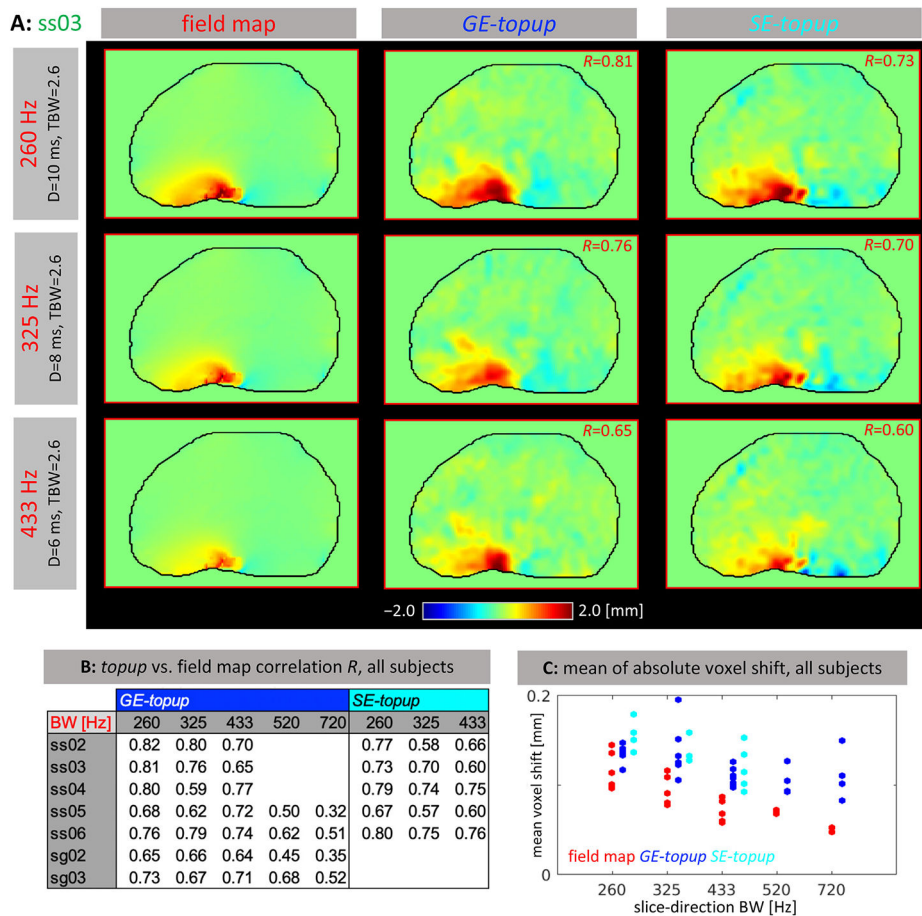
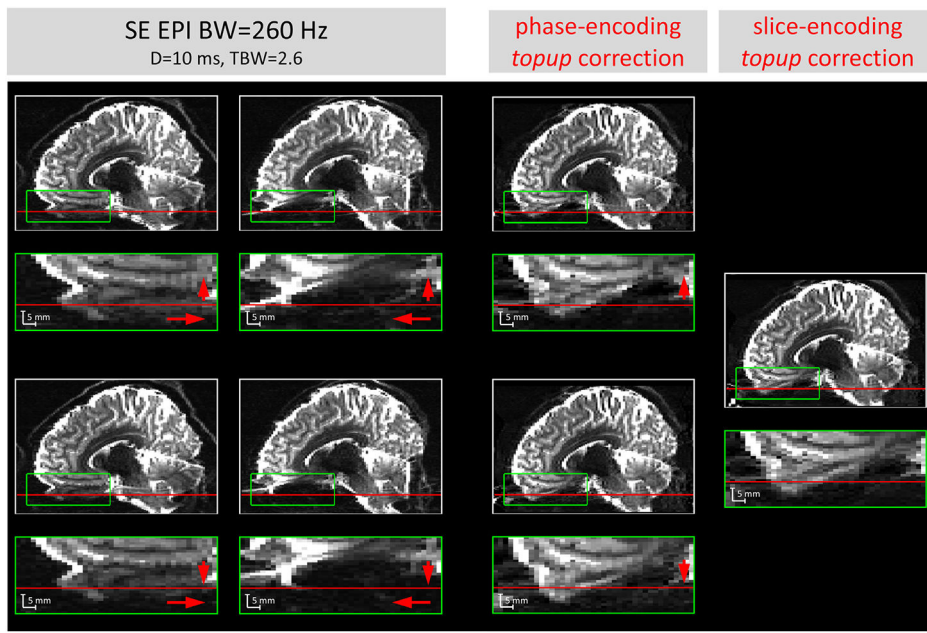


Fig. 3. Example sagittal reformats of gradient-echo (GE, left) and spin-echo (SE, right) EPI datasets from a representative subject (ss05), with 1-mm slice thickness and 1.5-mm in-plane resolution. Positive ($+G_z$, left) and negative ($-G_z$, right) slice-encoding direction (indicated by red arrows). The rows are ordered according to increasing slice-encoding BW values achieved by changing either the slice-select/slice-refocus pulse duration (D) or time-bandwidth product (TBW); see text for details. The horizontal red lines are included in the same position in each pair of images to help visualize shift of voxels due to distortion; magnified inserts correspond to a region indicated by the green box where distortion is pronounced. A summary of the data acquired for all remaining subjects is presented in Supplementary Fig. 2.

**Fig. 4.**

(A) Example sagittal reformats of voxel shift maps in the slice-encoding direction calculated for a representative subject (ss03) using the reverse-gradient-based (i.e., *topup*) (left) and conventional B_0 field map-based approach (middle) accompanied by the correlation coefficient calculated for each pair within the brain region (right). (B) Summary of the correlation coefficients calculated for pairs of the voxel shift maps across all subjects and BW values. (C) Comparison of *topup* and field map-based mean absolute voxel shift values for all subjects and BWs, with the blue points representing the voxel shift estimated from *topup* and the cyan points representing the corresponding voxel shift estimated from the B_0 field map.

**Fig. 5.**

Example sagittal reformats of the SE EPI dataset, acquired axially with 1-mm slice thickness, 2.0 mm in-plane resolution, A→P and P→A phase-encoding gradient direction (first and second column, respectively), positive and negative slice-encoding gradient direction (top and bottom row, respectively), slice-encoding pulse duration D=10 ms and TBW=2.6, which corresponds to BW=260 Hz; positive (+G_z) and negative (-G_z) slice-encoding direction, as well as A→P and P→A phase-encoding direction are indicated by red arrows; corresponding data distortion-corrected using *topup* method in phase-encoding direction (third column) and slice-encoding direction (fourth column); magnified inserts show distortion in the frontal sinus region with red horizontal line positioned in the same location in all panels.

Table 1

Summary of the EPI protocol parameters: TBW = time-bandwidth product in the slice-encoding direction, D = duration of a slice-encoding pulse, Gz = polarities of slice encoding, Gy = directions of phase-encoding gradient (where 'ap' stands for anterior-to-posterior and 'pa' stands for posterior-to-anterior), TH = slice thickness, RES = nominal in-plane voxel size, TR = repetition time, TE = echo time(s), FA = flip angle, ESP = nominal EPI echo spacing, R = in-plane acceleration factor, TA = time of acquisition, SL = number of slices, FOV = field of view. The right section of the table indicates which data were acquired for each of the subjects.

sequence	TBW	D [ms]	Gz	Gy	TH [mm]	RES [mm]	TR [ms]	TE(s) [ms]	FA [°]	ESP [ms]	R	TA	SL	FOV [mm]	ss02	ss03	ss04	ss05	ss06	Sg02	Sg03
EPI GRE	2.6	6/8/2010	pos/n eg	ap	1.0	1.5	5940	20	75	0.66	4	1:05	128	192 x 192							
EPI GRE	5.2/7.2	10	pos/n eg	ap	1.0	1.5	5940	20	75	0.66	4	1:05	128	192 x 192							
EPI SE	2.6	6/8/2010	pos/n eg	ap	1.0	1.5	15970	50	90	0.66	4	2:56	128	192 x 192							
EPI SE	2.6	10	pos/n eg	ap/p a	1.0	2.0	15970	50	90	0.66	2	2:08	128	192 x 192							
BO map	-	-	-	ap	2.0	2.0	570	3.0/4.02	46	-	-	1:52	128	192 x 192							